

Quantum Rotors on the AB₂ Chain with Competing Interactions

Antônio S. F. Tenório,¹ R. R. Montenegro-Filho,^{1,2} and M. D. Coutinho-Filho¹

¹*Laboratório de Física Teórica e Computacional, Departamento de Física,
Universidade Federal de Pernambuco, CEP 50670-901, Recife, Pernambuco, Brazil*

²*Escola Politécnica de Pernambuco, Universidade de Pernambuco, CEP 50750-470, Recife, Pernambuco, Brazil*

We present the ground state phase diagram of $q = 1/2$ quantum-rotor chains with competing interactions (frustration) calculated through cluster variational mean field approaches. We consider two interaction patterns, named F₁ and F₂ models, between the quantum-rotor momentum and position operators, which follow exchange patterns of known one-dimensional spin-1/2 systems with a ferrimagnetic state in their phase diagrams. The spin-1/2 F₁ model is known as the diamond chain and is related to the azurite compound, while the spin-1/2 F₂ model was recently shown to present a frustration-induced condensation of magnons. We provide a detailed comparison between the quantum-rotor phase diagrams, in single- and multi-site mean-field approaches, and known results for the spin-1/2 models, including exact diagonalization and density matrix renormalization group data for these systems, as well as phase diagrams of the associated classical models.

PACS numbers: 75.10.Pq, 75.10.Jm, 75.30.Kz, 75.40.Mg

I. INTRODUCTION

The connection between O(n) quantum-rotor (QR) and spin models on d -dimensional lattices has proved very useful in the context of phase transitions^{1,2}. About three decades ago, Hamer, Kogut and Susskind³ mapped two-dimensional O(n) Heisenberg models ($n = 2, 3$ and 4) onto the corresponding [(1+1) spatial and time dimensions] nonlinear-sigma or QR models. The critical behavior was then inferred using strong-coupling expansion (high-temperature, $g = kT/J \rightarrow \infty$, where J is the spin coupling): a Kosterlitz-Thouless transition for the O(2) model and a prediction of critical points at zero coupling (Padé continued) for both O(3) and O(4) models. On the other hand, by mapping O(3) antiferromagnetic (AF) Heisenberg chains onto nonlinear sigma models in the semiclassical weak-coupling limit ($g = 2/S, S \rightarrow \infty$), Haldane⁴ suggested that the ground state (GS) of chains with integral spins are gapped, while those with half-integral spins are gapless. Moreover, Shankar and Read⁵ precisely clarified the distinction between gapped AF spin models, characterized by the $\theta = 0 \bmod 2\pi$ topological term, and gapless models for which $\theta = \pi \bmod 2\pi$, including the connection of the latter with a Laplacian minimally coupled to the monopole potential⁶. Following the above developments, Sachdev and Senthil^{2,7} have presented a quite general mean-field and renormalization-group analysis of quantum phase transitions in magnets with the aid of *generalized* QR models. In particular, they showed that, under certain conditions, one can establish a mapping of double-layer antiferromagnets onto quantum rotors which sheds intuitive light on the way in which a QR can be used as an effective representation of a pair of antiferromagnetically coupled spins. Still in this context, a single-site MF approximation was used to study an effective Hamiltonian for spin-one bosons in an optical lattice in the presence of a magnetic field⁸. Further, a QR description of the Mott-insulator transition in the Bose-Hubbard model within a

functional-integral approach has also been elaborated in order to include particle number fluctuation effects⁹.

In this work we focus our attention on the study of the GS phase diagram of generalized quantum rotors on the frustrated AB₂ chain, which is depicted in Fig. 1. The quantum rotors at each site are constrained, through sufficiently high values of the coupling g (and the coupling α of the quartic term in the angular momentum), to mostly retain states with the minimum value of the angular momentum, i.e., $\ell = 1/2$, as the frustration parameter J is varied, thus enabling us to make a direct comparison with the corresponding *quantum* spin-1/2 AB₂ chains. We analyze two types of frustration, as illustrated in Fig. 1, and try to interpret the derived phase diagrams in light of the ones of previous works on frustrated quantum spin-1/2 chains with the AB₂ topology^{10–15}. Instead of attempting to formalize a specific (and probably rather complex) mapping between the rotor and the spin models, we have opted to treat the rotor chain numerically by using a cluster variational MF theory, supplemented with exact diagonalization (ED) via Lanczos algorithm¹⁶ and density matrix renormalization group (DMRG)¹⁷ of finite-size spin-1/2 chains.

With respect to spin systems, as a motivation on the experimental side, the compound azurite¹⁸ has been successfully explained by the distorted diamond chain model¹⁴, i.e., a system with three spin-1/2 magnetic sites per unit cell and frustrated ferrimagnetic state. Also, along with the study on the effect of frustration^{10–15}, for $J = 0$ this class of models shares its phenomenology and unit-cell topology with quasi-one-dimensional compounds, such as the line of trimer clusters present in copper phosphates¹⁹ and the organic ferrimagnet PNNBNO²⁰. The modeling of the ferrimagnetic phase²¹ has been mainly undertaken in the context of other models such as Hubbard²², $t - J^{23}$, Ising²⁴, classical²⁴ and quantum Heisenberg²⁵, including magnetic excitations^{26,27}, and the quantum spherical model²⁸. The occurrence of new phases induced by

hole-doping of the electronic band²⁹ has also been carried out.

This paper is organized as follows. In the next section we describe our QR model and numerical methods, and include in Appendix A a derivation of the matrix elements of the operators acting on the single-site Hilbert space represented by monopole harmonics. In Sec. III we use single-site variational MF theory to study the rotor models, for the two frustration cases, and discuss the shortcomings of this semiclassical approach. Then in Sec. IV we adopt a multi-site (two-unit cell) variational MF Hamiltonian, which provides a substantial improvement on the treatment of quantum fluctuation effects, particularly in connection with the case of frustrated interaction between quantum rotors on B sites at the same unit cell. Here we treat the respective spin-1/2 systems by making use of ED and DMRG techniques in order to pave the way for a direct comparison between rotors and spins. Finally we report our conclusions in Sec. V.

II. OUTLINE OF THE THEORY AND METHODS

Quantum rotors can be classified according to their minimum angular momentum^{6,7}: rotors with $q = 0$ have zero minimum angular momentum, which can be made to correspond to an even number of Heisenberg spins in an underlying spin model. On the other hand, we also have rotors with $q \neq 0$, where q is chosen to have one of the values: $1/2, 1, 3/2, \dots$, as will be briefly clarified below. This is an extension of the former case, and quantum rotors with half-integer values of q are duly suited to refer to an odd number of underlying spins-1/2 (at least one spin remains unpaired). We shall focus on $q = 1/2$ -quantum rotors in view of the stated objective of comparing our results with those for the referred chains of spin-1/2 operators.

The three-component unit vector (operator) $\hat{\mathbf{n}} = (\hat{n}_x, \hat{n}_y, \hat{n}_z)$, with $\hat{\mathbf{n}}^2 = 1$, describes the configuration space (n space) of a rotor, while $\hat{\mathbf{L}} = (\hat{L}_x, \hat{L}_y, \hat{L}_z)$ stands for the canonically conjugate angular momenta. Setting $\hbar \equiv 1$, these quantities obey the commutation relations (operators at different sites commute):

$$\begin{aligned} [\hat{L}_\mu, \hat{L}_\nu] &= i\epsilon_{\mu\nu\lambda}\hat{L}_\lambda, \\ [\hat{L}_\mu, \hat{n}_\nu] &= i\epsilon_{\mu\nu\lambda}\hat{n}_\lambda, \\ [\hat{n}_\mu, \hat{n}_\nu] &= 0, \end{aligned} \quad (1)$$

where the Greek letters stand for the Cartesian components x, y, z (summation over repeated indices is subtended and $\epsilon_{\mu\nu\lambda}$ is the Levi-Civita tensor) and

$$\hat{L}_\mu = -\epsilon_{\mu\nu\lambda}\hat{n}_\nu \left[i\frac{\partial}{\partial \hat{n}_\lambda} + qA_\lambda(\hat{n}_\mu) \right] - q\hat{n}_\mu, \quad (2)$$

which incorporates the effect of a Dirac monopole at the origin of n space, whose vector potential may be conveniently

chosen to satisfy

$$\epsilon_{\mu\nu\lambda}\partial A_\lambda/\partial \hat{n}_\nu = \hat{n}_\mu. \quad (3)$$

The appropriate Hilbert space is made up of *angular section* states for which the following are true⁶: $\hat{\mathbf{L}}^2|q, l, m\rangle = l(l+1)|q, l, m\rangle$; $\hat{L}_z|q, l, m\rangle = m|q, l, m\rangle$; and the usual ladder operators ($\hat{L}_\pm = \hat{L}_x \pm i\hat{L}_y$) satisfy $\hat{L}_\pm|q, l, m\rangle = \sqrt{(l \mp m)(l \pm m + 1)}|q, l, m \pm 1\rangle$. Here $l = q, q+1, q+2, \dots$, and $m = -l, -l+1, \dots, l$. The $|q, l, m\rangle$ are the eigensections, also called *monopole harmonics*. An important constraint follows immediately from Eq.(2):

$$\hat{\mathbf{n}} \cdot \hat{\mathbf{L}} = -q. \quad (4)$$

Thus, following Ref. 7, we shall consider the quite general frustrated O(3) QR Hamiltonian:

$$\begin{aligned} \hat{H}_R &= \frac{g}{2} \sum_i [(\hat{\mathbf{L}}_i^2 + \alpha(\hat{\mathbf{L}}_i^2)^2)] + \\ &\sum_{\langle ij \rangle} [\hat{\mathbf{n}}_i \cdot \hat{\mathbf{n}}_j + \hat{\mathbf{L}}_i \cdot \hat{\mathbf{L}}_j + M(\hat{\mathbf{n}}_i \cdot \hat{\mathbf{L}}_j + \hat{\mathbf{n}}_j \cdot \hat{\mathbf{L}}_i)] + \\ &\sum_{(i,j) \in F_1 \text{ or } F_2} [J(\hat{\mathbf{n}}_i \cdot \hat{\mathbf{n}}_j + \hat{\mathbf{L}}_i \cdot \hat{\mathbf{L}}_j) + M(\hat{\mathbf{n}}_i \cdot \hat{\mathbf{L}}_j + \hat{\mathbf{n}}_j \cdot \hat{\mathbf{L}}_i)], \end{aligned} \quad (5)$$

where g and α are positive local couplings, i.e., associated with rotors at each site i of the AB₂ chain (the quartic term appears with the main objective of controlling contributions of high-energy states); in the second summation, $\langle ij \rangle$ indexes nearest-neighbor couplings between rotors on distinct sublattices which, except for M , are all set to unity (see Fig. 1); in the third summation (i, j) indexes nearest-neighbor couplings between rotors on the same sublattice which, except for M , are set to $J(\geq 0)$. Here we shall study two frustration patterns, namely, F_1 and F_2 . In F_1 only frustrated interactions (J and M) between rotors at B sites of the same unit cell are present, as illustrated in Fig. 1(a), whereas for F_2 we consider *all* nearest-neighbor intra- and intercell interactions, as illustrated in Fig. 1(b). In order to isolate the effect of the coupling M in the two above-referred cases, we take either $M = 0$ or $M = 1$.

Before going on to the approaches described in Sec. III and Sec. IV, we emphasize the following features about the *stability* of the numerical implementations carried out in this work.

In our simulations we have verified that we could work safely with a minimally reduced Hilbert space if the values of g and α were set sufficiently large. In fact, the Hilbert space size and the value of g and α determine the stability of our problem: for small space sizes (e.g., $\ell = 3/2$) and small values of g and α (e.g., $g = \alpha = 0.1$), the system becomes completely unstable due to contributions of high-energy terms which cause the system to fluctuate beyond control. On the other hand, by choosing a small space size ($\ell = 3/2$), but a sufficiently large value of g , the system behaves quite stably. Therefore,

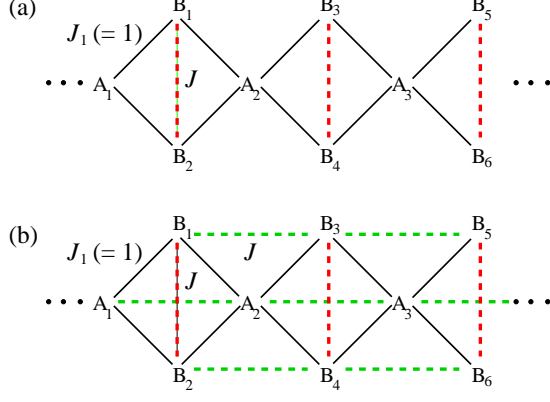


FIG. 1. (Color online) Illustration of the QR chains with three rotors per unit cell i : A_i , B_{2i-1} , and B_{2i} . Full lines indicate antiferromagnetic exchange couplings ($J_1 \equiv 1$) which give rise to the ferrimagnetic GS, while dashed lines represent exchange couplings ($J \geq 0$) which frustrate the magnetic order: (a) frustration pattern F_1 and (b) frustration pattern F_2 .

in this work we shall use small space size, i.e., $\ell = 3/2$, associated with a large value of g , in order to make computations feasible and a close contact with spin-1/2 models.

We then start off by treating \hat{H}_R by means of a variational MF theory based on the Bogoliubov theorem^{30,31}. Thus, the variational expression of the MF energy at $T = 0$ satisfies the inequality:

$$E_{mf} \leq E_0 + \langle \hat{H}_R - \hat{H}_{trial} \rangle, \quad (6)$$

where E_0 is the GS energy of the trial Hamiltonian - here denoted by \hat{H}_{trial} - and the expectation value is taken with respect to its GS wavefunction. Eq. (6) is then minimized with respect to its variational parameters: for chosen values of the frustration control parameter (J), minimization is carried out numerically through diagonalization of \hat{H}_{trial} by way of the Lanczos algorithm¹⁶, and then deploying a simplex procedure³².

For trial Hamiltonians we use both single-site and multi-site Hamiltonians, as described in Sec. III and Sec. IV, respectively.

III. QUANTUM ROTORS ON THE AB_2 CHAIN: SINGLE-SITE VARIATIONAL MEAN-FIELD APPROACH ON THE UNIT CELL

As a first and straightforward application of the aforementioned variational MF theory, we postulate the following trial Hamiltonian, acting on one unit cell:

$$\hat{H}_{trial} = \frac{g}{2} \sum_i [(\hat{\mathbf{L}}_i^2 + \alpha(\hat{\mathbf{L}}_i^2)^2) + \mathbf{N}_i \cdot \hat{\mathbf{n}}_i + \mathbf{h}_i \cdot \hat{\mathbf{L}}_i], \quad (7)$$

where $\mathbf{h} = (h_x, h_y, h_z)$ and $\mathbf{N} = (N_x, N_y, N_z)$ are the variational c-number fields and the subscript i goes over the sites A_1 , B_1 , and B_2 .

The GS wavefunction of \hat{H}_{trial} and energy are given by $|\Psi_0\rangle = |\Psi_0\rangle_{A_1} |\Psi_0\rangle_{B_1} |\Psi_0\rangle_{B_2}$ and $E_0 = \sum_i E_{0i} = E_{0A_1} + E_{0B_1} + E_{0B_2}$, where $E_{0i} = E_{0i}(g, \alpha; N_i, h_i)$ represents the GS energy of the respective wavefunction, such that for any pair of operators $\hat{\mathbf{X}}_i, \hat{\mathbf{X}}_j$, with $i \neq j$:

$$\langle \Psi_0 | \hat{\mathbf{X}}_i \cdot \hat{\mathbf{X}}_j | \Psi_0 \rangle = \langle \hat{\mathbf{X}}_i \rangle_0 \cdot \langle \hat{\mathbf{X}}_j \rangle_0, \quad (8)$$

We then get, for frustration F_1 , the Bogoliubov inequality for the unit cell: $E_{mf}^{(F_1)} \leq E_1 + E_2 + E_3$, where the E_ν read:

$$E_1 = \sum_i E_{0i} - \sum_i (\mathbf{N}_i \cdot \langle \hat{\mathbf{n}}_i \rangle_0 + \mathbf{h}_i \cdot \langle \hat{\mathbf{L}}_i \rangle_0);$$

$$E_2 = 2 \sum_{i>j, j=A_1} [\langle \hat{\mathbf{n}}_i \rangle_0 \cdot \langle \hat{\mathbf{n}}_j \rangle_0 + \langle \hat{\mathbf{L}}_i \rangle_0 \cdot \langle \hat{\mathbf{L}}_j \rangle_0 + M(\langle \hat{\mathbf{n}}_i \rangle_0 \cdot \langle \hat{\mathbf{L}}_j \rangle_0 + \langle \hat{\mathbf{n}}_j \rangle_0 \cdot \langle \hat{\mathbf{L}}_i \rangle_0)];$$

and

$$E_3 = J(\langle \hat{\mathbf{n}}_{B_1} \rangle_0 \cdot \langle \hat{\mathbf{n}}_{B_2} \rangle_0 + \langle \hat{\mathbf{L}}_{B_1} \rangle_0 \cdot \langle \hat{\mathbf{L}}_{B_2} \rangle_0) + M(\langle \hat{\mathbf{n}}_{B_1} \rangle_0 \cdot \langle \hat{\mathbf{L}}_{B_2} \rangle_0 + \langle \hat{\mathbf{n}}_{B_2} \rangle_0 \cdot \langle \hat{\mathbf{L}}_{B_1} \rangle_0);$$

the index i (j) visits the sites of the unit cell, with the convention: $A_1 < B_1 < B_2$. For frustration F_2 , a fourth term must be added to the Bogoliubov inequality:

$$E_4 = 2 \sum_i [J \langle \hat{\mathbf{n}}_i \rangle_0 \cdot \langle \hat{\mathbf{n}}_i \rangle_0 + \langle \hat{\mathbf{L}}_i \rangle_0 \cdot \langle \hat{\mathbf{L}}_i \rangle_0 + M(\langle \hat{\mathbf{n}}_i \rangle_0 \cdot \langle \hat{\mathbf{L}}_i \rangle_0 + \langle \hat{\mathbf{n}}_i \rangle_0 \cdot \langle \hat{\mathbf{L}}_i \rangle_0)].$$

The MF energy - best evaluation of $E_{mf}^{(F_1)} \equiv E_{mf}^{(F_1)}(g, \alpha, J)$ or $E_{mf}^{(F_2)} \equiv E_{mf}^{(F_2)}(g, \alpha, J)$ - is then obtained by performing the minimization with respect to variations of the fields \mathbf{N}_i and \mathbf{h}_i .

To produce the results of this section, it sufficed to set $g = \alpha = 10$ and a space size determined by truncating the Hilbert space at $\ell = 3/2$. Further, we have focused only on those quantities that suffice to afford the relevant information needed for the proper interpretation of the problem at this level, i. e., the two-point MF momentum products, defined here through the products $\langle \hat{\mathbf{L}}_i \rangle \cdot \langle \hat{\mathbf{L}}_j \rangle$, where $i \neq j$ runs over the sites of the unit cell, and the MF energy. We thereby leave out the position- and momentum-position products, for they are redundant. This is due to the fact that \hat{L}_μ and \hat{n}_μ have the same signature under all allowed symmetries for $q \geq 0$, and so their expectation values turn out to be proportional to each other on a given site⁷.

We then proceed to discuss the results in Fig. 2 (frustration F_1) and Fig. 3 (frustration F_2), which reveal some salient features. Firstly, we verified that $\langle \hat{\mathbf{L}}_i \rangle^2 = 0.25$, with $i = A_1, B_1, B_2$, independent of J . The momentum products show that, in all cases, the system starts out with a magnetization plateau: $\langle \hat{\mathbf{L}}_{B_1} \rangle \cdot \langle \hat{\mathbf{L}}_{B_2} \rangle = 0.25$ and $\langle \hat{\mathbf{L}}_{A_1} \rangle \cdot \langle \hat{\mathbf{L}}_{B_{1,2}} \rangle = -0.25$, which corresponds to the Lieb-Mattis³³ phase of the analogous spin-1/2 system,

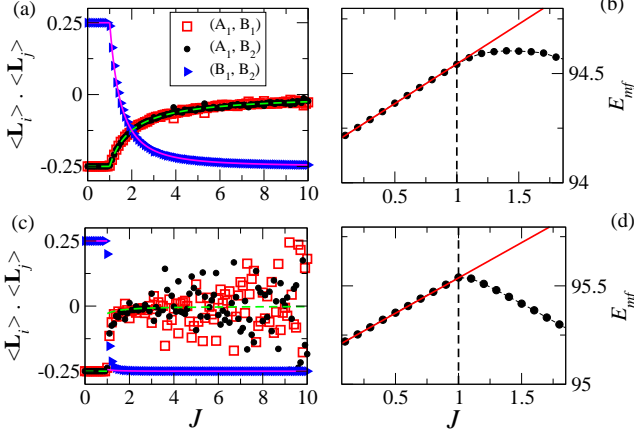


FIG. 2. (Color online) Frustration F_1 . Two-point MF momentum products [(a) $M \equiv 0$, (c) $M \equiv 1$] between the indicated rotors and MF energy curve [(b) $M \equiv 0$, (d) $M \equiv 1$], where we have drawn straight (full) lines to show that at $J = 1$ the system steers away from the linear regime that prevails for $J \leq 1$ and so a phase transition takes place. Full and dashed lines in (a) and (c) indicate the results of the classical vector model. Dashed lines in (b) and (d) are guides to the eye.

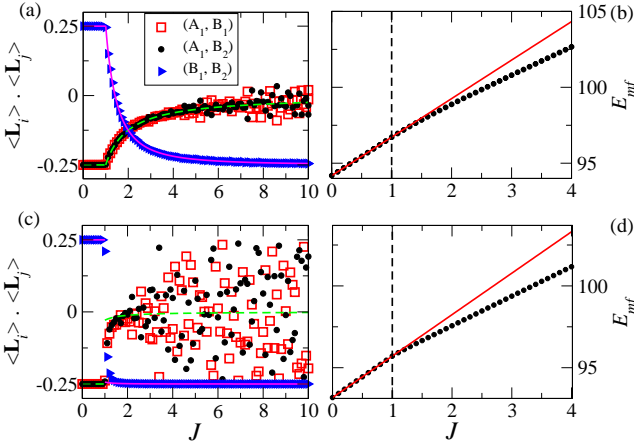


FIG. 3. (Color online) Frustration F_2 . Same as in Fig. 2.

before undergoing a phase transition at $J = 1$. This transition is of second order ($M \equiv 0$), as shown in Fig. 2 (a) and Fig. 3 (a), and of first order ($M \equiv 1$), as shown in Fig. 2 (c) and Fig. 3 (c).

In the first case ($M \equiv 0$), the system evolves continually (with the MF energy curve - Fig. 2 (b) and Fig. 3 (b) - smooth at the point $J = 1$) to a stable phase where the momenta at A and B sites become uncorrelated, i.e., $\langle \hat{\mathbf{L}}_{A_1} \rangle \cdot \langle \hat{\mathbf{L}}_{B_{1,2}} \rangle \approx 0$, while the momenta at B sites tend to directly oppose each other with increasing J , forming a singlet-like configuration: $\langle \hat{\mathbf{L}}_{B_1} \rangle \cdot \langle \hat{\mathbf{L}}_{B_2} \rangle \approx -0.25$, for $J \gg 1$.

In the second case ($M \equiv 1$), the transition takes place

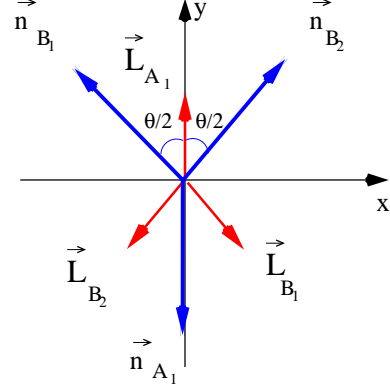


FIG. 4. (Color online) Classical vector configuration. The angle θ is the unique order parameter.

quite abruptly, having undoubtedly first-order characteristics, and the system immediately accommodates into the stable singlet-like phase that we have just referred to. The MF energy curves of these first-order transitions at $J = 1$ are shown in Fig. 2 (d) and Fig. 3 (d), where we notice that the cusp in the latter is less pronounced.

We notice further, that the products between the momenta at A and B sites display quite sizable fluctuations around $\langle \hat{\mathbf{L}}_{A_1} \rangle \cdot \langle \hat{\mathbf{L}}_{B_{1,2}} \rangle \approx 0$, as seen in Fig. 2 (c) and Fig. 3 (c) ($M \neq 0$), and in lesser degree in Fig. 3 (a) for frustration F_2 and $M = 0$. The corresponding wide points occur pairwise and fairly symmetrically with respect to classical curves (see below) that represent the decoupling of the momenta at A and B sites, leaving the MF energy practically unaltered. In fact, with increasing J , the system becomes more prone to wandering through near-degenerate states, which give rise to these off points.

The phase, for $J \gg 1$, with A sites uncoupled and B sites with opposing momenta in a singlet-like configuration is much like the dimer-monomer phase of the work by Takano, Kubo, and Sakamoto¹⁰. We perceive, however, that important features in between those J extremes of the phase diagram do not appear by way of this naive *single-site* MF theory.

We now notice, through Eq. (8), that with the rotor momenta being fixed at $\ell = 1/2$, we have $\langle L_i \rangle^2 = 0.25$, for all sites i , independent of J , and so all products can only vary between the extremes -0.25 and 0.25. Therefore, through this MF approach, we are led to envision the momenta on the unit cell of the AB_2 chain as classical vectors of constant magnitude, such as represented in Fig. 4. We can thus provide a simple interpretation based on this configuration of classical vectors on the xy plane (akin to the xy -model). We then build our energy function for the configuration in Fig. 4 ($\alpha \equiv 0$) on a symmetric unit of the AB_2 chain centered on the A site. The classical constraints may be set as $|\mathbf{L}_{A_1}| = |\mathbf{L}_{B_1}| = |\mathbf{L}_{B_2}| \equiv 1/2$ and $|\mathbf{n}_{A_1}| = |\mathbf{n}_{B_1}| = |\mathbf{n}_{B_2}| \equiv n$ (we take n constant, which is about true for small ℓ , as verified in the simulations, and whose value must

be read off from the plots). We start off with the energy function for the frustration F_1 , taking into account the cases $M = 0$ and $M = 1$. So, for each case, up to a constant independent of θ : $E_{(M=0)}(\theta) = -2(1 + 4n^2) \cos \frac{\theta}{2} + \frac{J}{2}(1 + 4n^2) \cos \theta$ and $E_{(M=1)}(\theta) = -2(1 - 4n + 4n^2) \cos \frac{\theta}{2} - 2n \cos \theta + \frac{J}{2}(1 + 4n^2) \cos \theta$. Upon imposing the minimization conditions (relative to the unique parameter θ), we obtain: (i) for $J < 1$ we have $\theta = 0$, which holds for both $M = 0$ and $M = 1$; (ii) for $J > 1$, we have $\theta \neq 0$, which in turn implies that $J = \frac{1}{\cos \frac{\theta}{2}}$, for $M = 0$, while $J = \frac{(1-2n)^2 + 4n \cos \frac{\theta}{2}}{(1+4n^2) \cos \frac{\theta}{2}}$, for $M = 1$. The momentum products are accordingly given by: for $J < 1$, $\mathbf{L}_{A_1} \cdot \mathbf{L}_{B_{1,2}} = -0.25$ and $\mathbf{L}_{B_1} \cdot \mathbf{L}_{B_2} = +0.25$, for both $M = 0$ and $M = 1$. For $J > 1$,

$$\begin{aligned} \mathbf{L}_{A_1} \cdot \mathbf{L}_{B_{1,2}} &= -\frac{1}{4J}, \\ \mathbf{L}_{B_1} \cdot \mathbf{L}_{B_2} &= \frac{1}{2J^2} - \frac{1}{4}, \quad M = 0; \end{aligned} \quad (9)$$

$$\begin{aligned} \mathbf{L}_{A_1} \cdot \mathbf{L}_{B_{1,2}} &= -\frac{1}{4} \left(\frac{(1-2n)^2}{J(1+4n^2) - 4n} \right), \\ \mathbf{L}_{B_1} \cdot \mathbf{L}_{B_2} &= \frac{1}{4} \left(\frac{2(1-2n)^4}{[J(1+4n^2) - 4n]^2} - 1 \right), \quad M = 1. \end{aligned} \quad (10)$$

With respect to frustration F_2 , our present MF approach can only “sense” a repetition of the configuration of Fig. 4, in that we get additional terms to the energy functions above that are independent of θ (and therefore vanish upon minimization), implying the same results for the dot products.

This classical description fully accounts for the momentum products in both frustration types for $M = 0$, including the nature of the phase transition at $J = 1$, as seen in Fig. 2(a) and Fig. 3(a) through the matching fitting of the points of the numerical implementation for the rotors; for $M = 1$, this interpretation confirms the first-order transition at $J = 1$ and offers hints at the expected behavior of these momentum products, were it not for the off points, as can be seen in the diagrams of Fig. 2(c) and Fig. 3(c). In Eq. (10) we have used $n = 0.34$, that can be read off from plots of $\langle \hat{\mathbf{n}}^2 \rangle$, which were not explicitly presented in this work.

In the following section we try a *more elaborate* MF technique on a double-cell structure, as a way to circumvent Eq. (8), as well as to get a direct evaluation of the intercell two-point correlations. For simplicity, we restrict ourselves to $M = 0$.

IV. QUANTUM ROTORS ON THE AB_2 CHAIN: DOUBLE-CELL VARIATIONAL MEAN-FIELD APPROACH

Differently from the approach presented in Sec. III, we build our trial Hamiltonian acting on the *global* space formed by the six sites of the double-cell structure made

up of two contiguous unit cells, such as showed in Fig. 1, i.e., we build one *six-site* trial Hamiltonian acting, say, on the sites A_1, A_2, B_1, B_2, B_3 , and B_4 . In order to achieve that, we assigned to each site its own *local* vector subspace, and we then constructed our global space by forming the tensor product of these subspaces in one chosen order. In order to simplify the equations below, when necessary, the *local* operator acting on the QR located at site A_1 , for instance, was denoted by $\hat{\mathbf{X}}_{A_1}$, which may refer to either operator $\hat{\mathbf{L}}$ or operator $\hat{\mathbf{n}}$.

We now write down the trial Hamiltonian acting on a given double-cell structure for frustration F_1 :

$$\hat{H}_{trial} = \hat{H}_{trial}^{(1)} + \hat{H}_{trial}^{(2)} + \hat{H}_{trial}^{(3)}. \quad (11)$$

The first term (the kinetic energy term plus effective fields) is given by

$$\hat{H}_{trial}^{(1)} = \frac{g}{2} \sum_i [(\hat{\mathbf{L}}_i)^2 + \alpha((\hat{\mathbf{L}}_i)^2)^2 + \mathbf{N}_i \cdot \hat{\mathbf{n}}_i + \mathbf{h}_i \cdot \hat{\mathbf{L}}_i], \quad (12)$$

where the index i goes over the sites A_1, A_2, B_1, B_2, B_3 , and B_4 ; \mathbf{N}_i and \mathbf{h}_i being the effective fields (variational c-numbers) due to the rest of the system (which plays the role of a bath), and acting on each site i of the double-cell cluster. The next term (first neighbors or bonds) reads

$$\begin{aligned} \hat{H}_{trial}^{(2)} &= \sum_{\hat{\mathbf{X}}=\hat{\mathbf{n}}, \hat{\mathbf{L}}} [(\hat{\mathbf{X}}_{A_1} + \hat{\mathbf{X}}_{A_2}) \cdot (\hat{\mathbf{X}}_{B_1} + \hat{\mathbf{X}}_{B_2}) \\ &\quad + \hat{\mathbf{X}}_{A_2} \cdot (\hat{\mathbf{X}}_{B_3} + \hat{\mathbf{X}}_{B_4})], \end{aligned} \quad (13)$$

while the last one (frustration interaction) is written as

$$\hat{H}_{trial}^{(3)} = J \sum_{\hat{\mathbf{X}}=\hat{\mathbf{n}}, \hat{\mathbf{L}}} [(\hat{\mathbf{X}}_{B_1} \cdot \hat{\mathbf{X}}_{B_2}) + (\hat{\mathbf{X}}_{B_3} \cdot \hat{\mathbf{X}}_{B_4})], \quad (14)$$

where in the first term we opted to use explicit operators.

For frustration F_2 , the following term (intercell frustration interaction) must be added to Eq. (11):

$$\hat{H}_{trial}^{(4)} = J \sum_{\hat{\mathbf{X}}=\hat{\mathbf{n}}, \hat{\mathbf{L}}} [(\hat{\mathbf{X}}_{A_1} \cdot \hat{\mathbf{X}}_{A_2} + \hat{\mathbf{X}}_{B_1} \cdot \hat{\mathbf{X}}_{B_3} + \hat{\mathbf{X}}_{B_2} \cdot \hat{\mathbf{X}}_{B_4})]. \quad (15)$$

The direct application of Eq. (6) yields for frustration F_1 the following expression for the *double-cell* variational MF energy $E_{mf}^{(F1)} \equiv E_{mf}^{(F1)}(g, \alpha, J)$, where the equals sign implies that minimization with respect to the variational fields has already been carried out:

$$\begin{aligned} E_{mf}^{(F1)} &= E_0 + \sum_{\hat{\mathbf{X}}=\hat{\mathbf{n}}, \hat{\mathbf{L}}} \langle \hat{\mathbf{X}}_{A_1} \rangle_0 \cdot (\langle \hat{\mathbf{X}}_{B_3} \rangle_0 + \langle \hat{\mathbf{X}}_{B_4} \rangle_0) \\ &\quad - \sum_i (\mathbf{N}_i \cdot \hat{\mathbf{n}}_i + \mathbf{h}_i \cdot \hat{\mathbf{L}}_i), \end{aligned} \quad (16)$$

where, E_0 represents the GS energy of \hat{H}_{trial} and, as before, the index i visits the sites A_1, A_2, B_1, B_2, B_3 , and B_4 .

For frustration F_2 , we get analogously $E_{mf}^{(F2)} = E_{mf}^{(F2)}(g, \alpha, J)$:

$$\begin{aligned}
E_{mf}^{(F2)} = E_0 + \sum_{\hat{\mathbf{X}}=\hat{\mathbf{n}}, \hat{\mathbf{L}}} & \langle \hat{\mathbf{X}}_{A_1} \rangle \cdot (\langle \hat{\mathbf{X}}_{B_3} \rangle + \langle \hat{\mathbf{X}}_{B_4} \rangle) \\
& + 2J \sum_{\hat{\mathbf{X}}=\hat{\mathbf{n}}, \hat{\mathbf{L}}} (\langle \hat{\mathbf{X}}_{A_1} \rangle \cdot \langle \hat{\mathbf{X}}_{A_2} \rangle + \\
& \langle \hat{\mathbf{X}}_{B_1} \rangle \cdot \langle \hat{\mathbf{X}}_{B_3} \rangle + \langle \hat{\mathbf{X}}_{B_2} \rangle \cdot \langle \hat{\mathbf{X}}_{B_4} \rangle) \\
& - \sum_i (\mathbf{N}_i \cdot \hat{\mathbf{n}}_i + \mathbf{h}_i \cdot \hat{\mathbf{L}}_i). \quad (17)
\end{aligned}$$

Now, a given eigenfunction of \hat{H}_{trial} may not necessarily be a tensor product of the eigenfunctions of the respective site subspaces as was the case in Sec. III, so that, for example,

$$\langle \Psi_0 | \hat{\mathbf{X}}_{A_1} \cdot \hat{\mathbf{X}}_{B_2} | \Psi_0 \rangle \neq \langle \Psi_0 | \hat{\mathbf{X}}_{A_1} | \Psi_0 \rangle \cdot \langle \Psi_0 | \hat{\mathbf{X}}_{B_2} | \Psi_0 \rangle, \quad (18)$$

where $|\Psi_0\rangle$ designates the GS wavefunction of H_{trial} . This is an important aspect in our approach, which differs from the standard MF result given by Eq. (8). Thus, in principle, taking advantage of the available capability of diagonalizing more complex operators (trial Hamiltonians), we can produce more reliable cluster variational MF theories.

The dimension of the global space is d^6 , where d is the dimension of the local subspace, so due to computational implementability, this fact prompted us to limit the size of the Hilbert space by deploying rotors with maximum $\ell = 3/2$.

An observation about the value of g is in order. In our approach, for frustration F_1 , when we had set $g = 10$ as in the preceding section, we verified that the momentum correlation $\langle \hat{\mathbf{L}}_{A_1} \cdot \hat{\mathbf{L}}_{A_2} \rangle$ remains pegged at 0.25, even after the transition at $J = 2$, which turns out not to be true (see below). Therefore, in this section, we resorted to a higher value of g ($g = 1000$), which inhibited more strongly the appearance of disturbing states; however one should notice that if much greater values of g are employed, the kinetic energy becomes overwhelmingly dominant, so that small changes in the correlations tend to go unnoticed.

As before, we concentrated on the relevant quantities that can provide the information needed for the physical interpretation of the problem: namely, *the mean-field energy*, *the expectation value of the total angular momentum*, and *the momentum correlations*. The expectation value of the total angular momentum per unit cell was calculated according to the formula $|\langle \mathbf{L} \rangle|^2 = 1/2 \sum_{\mu} \langle L_{\mu}^2 \rangle$, where L_{μ} ($\mu = x, y, z$) is the respective resultant component (component sum over all the six sites of the double-cell structure).

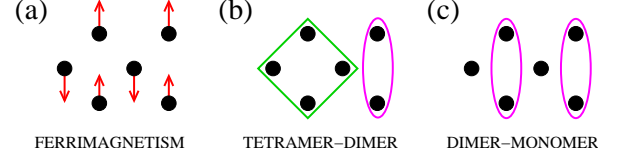


FIG. 5. (Color online) Illustration of the ground-states found for the spin-1/2 diamond chain¹⁰ as J is increased from 0. (a) The ferrimagnetic (FERRI) state. (b) The tetramer-dimer (TD) state, where rectangles represent singlet tetramers and ellipses singlet dimers. (c) The dimer-monomer (DM) state. There are two first-order phase transitions: at $J = 0.909$ (FERRI/TD) and $J = 2$ (TD/DM).

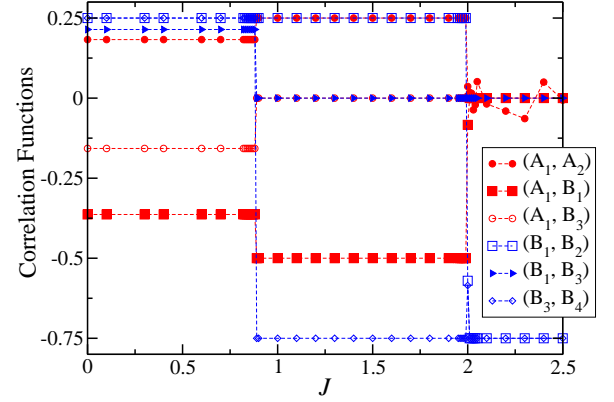


FIG. 6. (Color online) Spin-1/2 diamond chain: ED results for the correlation functions between spins at a central cluster of a system with 28 sites. Dashed lines are guides to the eye.

A. Frustration F_1

In order to facilitate comparison between QR results and those for the spin-1/2 counterpart with the same type of frustration, we present in Fig. 5 the phases obtained for the spin-1/2 diamond chain¹⁰. The Lieb-Mattis³³ ferrimagnetic phase (FERRI) appears when $J < 0.909$ (J is also used to indicate the frustration control parameter for the spin system). In the tetramer-dimer (TD) phase, which ensues when $0.909 < J < 2$, the state is precisely the regular array of singlet tetramers (the closed loop encompasses four spins, in which the B sites form a triplet pair, and the spins on the A sites oppose those on the B sites, so that zero total spin takes place), and singlet dimers (two spins within the elliptical contour) as shown in Fig. 5 (b). Finally, the dimer-monomer (DM) state is shown in Fig. 5 (c) and sets in when $J > 2$; it is composed of the regular array of singlet dimers and free spins, and vanishing total spin is also expected. Because of the free spins, the DM state is macroscopically $2^{N/3}$ -fold degenerate for a chain with N sites. Furthermore, both transitions are of first order¹¹.

In order to allow a direct comparison with our MF results for quantum rotors, we have solved the spin-1/2

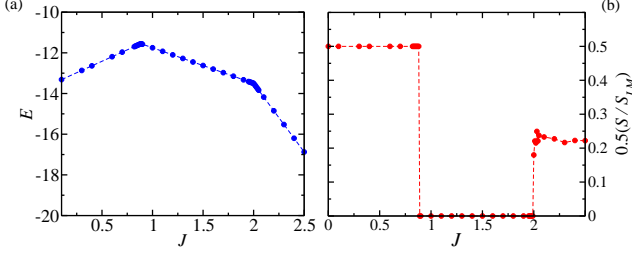


FIG. 7. (Color online) Spin-1/2 diamond chain: ED results for the (a) average ground-state energy and (b) rescaled total spin of a system with 28 sites. Phase transitions occur at $J = 0.88$ and $J = 2.0$, both of first order. Dashed lines are guides to the eye.

diamond chain (AB_2 chain with frustration between spins at sites B of the same unit cell) for sizes up to 28 sites, using the Lanczos ED procedure with open boundary conditions. The results are displayed as follows: the relevant correlations are represented by the curves plotted in Fig. 6; in Fig. 7 (a) and (b) we plotted respectively the energy and total-spin curves (normalized by the Lieb-Mattis value³³).

Examination of the correlation plots show clear correspondence with the phases exhibited in Fig. 5. The phase FERRI is characterized by the following correlations: $\langle \hat{S}_{B_1} \cdot \hat{S}_{B_2} \rangle = \langle \hat{S}_{B_3} \cdot \hat{S}_{B_4} \rangle = 0.25$, $\langle \hat{S}_{B_1} \cdot \hat{S}_{B_3} \rangle = 0.21$, $\langle \hat{S}_{A_1} \cdot \hat{S}_{A_2} \rangle = 0.18$, $\langle \hat{S}_{A_1} \cdot \hat{S}_{B_3} \rangle = -0.15$, $\langle \hat{S}_{A_1} \cdot \hat{S}_{B_1} \rangle = -0.36$. The total spin per unit cell in Fig. 7 (b) shows the Lieb-Mattis value of 0.5 throughout. The transition to the intermediate phase TD then occurs at $J = 0.88$, very close to the estimated value for the infinite chain¹⁰: $J = 0.909$. We note that in this phase the chain breaks up into smaller units - tetramers and dimers - and quantum fluctuations within each unit do not affect the spin correlations. Hence the correlations are just those calculated for the TD configuration of spins in Fig. 5 (b): $\langle \hat{S}_{A_1} \cdot \hat{S}_{A_2} \rangle = \langle \hat{S}_{B_1} \cdot \hat{S}_{B_2} \rangle = 0.25$ (triplets), $\langle \hat{S}_{B_3} \cdot \hat{S}_{B_4} \rangle = -0.75$ (singlets), $\langle \hat{S}_{A_1} \cdot \hat{S}_{B_1} \rangle = -0.5$, the other correlations being zero. With increasing J though, quantum fluctuations become strong enough to disrupt the tetramer unit and a new phase transition to DM phase happens at $J = 2$, this point being independent of size because of the chain breakup. In this phase correlation $\langle \hat{S}_{A_1} \cdot \hat{S}_{A_2} \rangle$ has varying nonzero values and does not vanish, as expected in the thermodynamic limit, due to finite size effects. On the other hand, the B spins, which are interlocked in singlet units, are totally unaffected. This phase, depicted in Fig. 5 (c), shows the final chain breakup as the tetramer gives way to two monomer units and another dimer, clearly indicated by the correlations in Fig. 6 ($J \geq 2$). The energy curve in Fig. 7 (a) exhibits cusps at the transition points, typical of a first-order nature, also verified through the discontinuities of the correlations at these points. The

total spin per unit cell in Fig. 7 (b) corroborates the above phase description; however in the last phase the apparent nonzero value is a finite-size effect.

Finally, getting down to the QR AB_2 chain, we display our variational MF numerical results in Fig. 8 (momentum correlations) and Fig. 9 (energy and total angular momentum) and we proceed to a comparative examination with respect to the preceding spin results. A blow-by-blow confrontation of the correlations in both Fig. 6 and Fig. 8 shows that the double-cell variational MF approach is able to reproduce the three phases exhibited in Ref. 10, namely, the FERRI, TD, and DM phases. In the FERRI phase, quantum fluctuations appear to be equally important, causing the same correlations to deviate somewhat from calculated results for stiff momenta. A closer examination shows that, up to two decimal digits, we have same correlations for $\langle \hat{L}_{B_1} \cdot \hat{L}_{B_2} \rangle = \langle \hat{L}_{B_3} \cdot \hat{L}_{B_4} \rangle = 0.25$, but slightly different correlations, namely: $\langle \hat{L}_{A_1} \cdot \hat{L}_{A_2} \rangle = 0.22$, $\langle \hat{L}_{A_1} \cdot \hat{L}_{B_1} \rangle = 0.46$, $\langle \hat{L}_{A_1} \cdot \hat{L}_{B_3} \rangle = 0.20$, and $\langle \hat{L}_{B_1} \cdot \hat{L}_{B_3} \rangle = 0.22$, for the rotor system, which should be compared with $\langle \hat{S}_{A_1} \cdot \hat{S}_{A_2} \rangle = 0.18$, $\langle \hat{S}_{A_1} \cdot \hat{S}_{B_1} \rangle = 0.36$, $\langle \hat{S}_{A_1} \cdot \hat{S}_{B_3} \rangle = 0.16$, and $\langle \hat{S}_{B_1} \cdot \hat{S}_{B_3} \rangle = 0.21$, for the spin system. Phase transitions occur at $J = 0.68$ and $J = 2$, evidently of first order; in the first transition we have a lesser value ($J = 0.68$) than the Lanczos result for the 28-site spin-1/2 chain ($J = 0.88$), and that of Ref. 10 ($J = 0.909$). The momentum and spin correlations match one another, respectively, in both phases: in the DM phase, correlation $\langle \hat{L}_{A_1} \cdot \hat{L}_{A_2} \rangle$ shows also an erratic behavior similar to its spin counterpart, in other words, finite size effects are also at play. The minor differences in correlations in the FERRI phase, as well as in the first transition point do not constitute a fundamental discrepancy between the respective phase diagrams, which are endowed with the same topological features. In Fig. 9 (a) the cusps in the mean-field energy at $J = 0.68$ and $J = 2$ also bespeak the occurrence of these first-order transitions. Comparing the total momentum in Fig. 9 (b) with the total spin in Fig. 7 (b), we observe similar results for the Lanczos predictions for the spin model, including finite-size effects in the last phase.

It is instructing to study the QR system regarding the average singlet density per unit cell of the B momenta¹², which in our case (*double-cell cluster*) is calculated directly using

$$\langle \eta \rangle = \frac{1}{4} - \frac{1}{2} (\langle \hat{L}_{B_1} \cdot \hat{L}_{B_2} \rangle + \langle \hat{L}_{B_3} \cdot \hat{L}_{B_4} \rangle), \quad (19)$$

and which is displayed in Fig. 10. These results permit a direct comparison with the phase diagram of Fig. 5, as far as the buildup of singlet pairs out of B momenta is concerned. As is the case for spins, size effects are not important here, so that one perceives that the number of singlets is very clearly a quantized quantity within each phase.

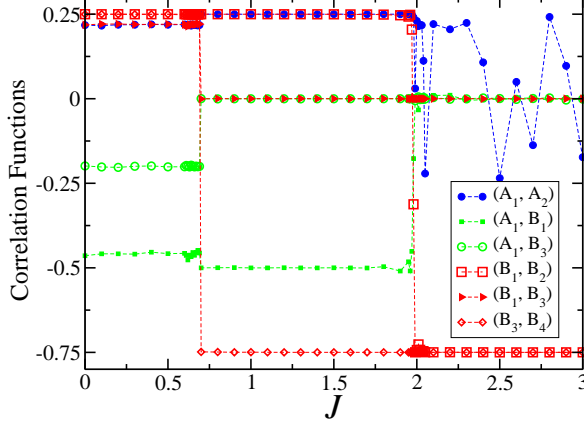


FIG. 8. (Color online) QR momentum correlations calculated by using the double-cell variational MF approach for frustration F_1 . One notices the phase sequence FERRI \leftrightarrow TD \leftrightarrow DM, with first-order transitions at $J = 0.68$ and $J = 2$. Dashed lines are guides to the eye.

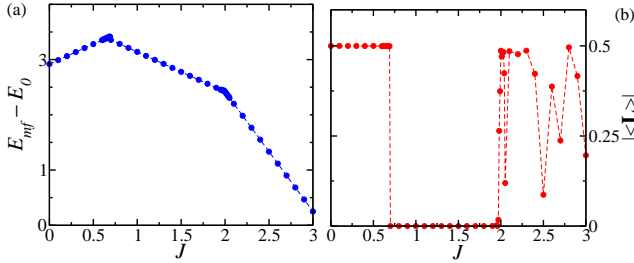


FIG. 9. (Color online) Quantum rotors by using the double-cell variational MF results for frustration F_1 : (a) the energy plot ($E_0 = 1962$) shows cusps at the first-order transition points $J = 0.68$ and $J = 2.0$; (b) expectation value of the total angular momentum per unit cell. Dashed lines are guides to the eye.

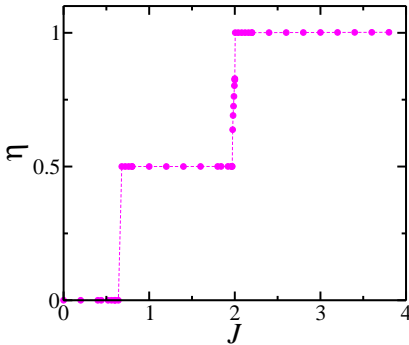


FIG. 10. (Color online) Quantum rotors with frustration F_1 : average singlet density per unit cell for the momenta of the B sites at the same unit cell. One can make out the three phases: FERRI, TD, and DM, as well as pertinent transitions. Dashed lines are guides to the eye.

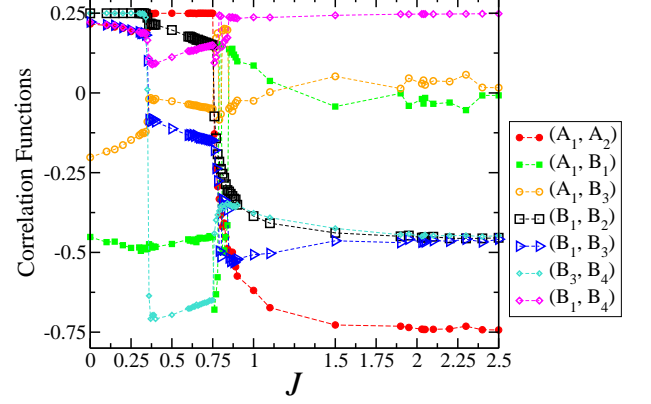


FIG. 11. (Color online) QR momentum correlations calculated by using the double-cell variational MF approach for frustration F_2 . One can distinguish three major phases: FERRI, CANTED, and the decoupled AF chain ladder system, with transitions occurring around $J = 0.35$ and $J = 0.75$. Dashed lines are guides to the eye.

B. Frustration F_2

Before getting down to quantum rotors, we describe succinctly existent results¹² for the spin-1/2 AB_2 chain with the same frustration F_2 pattern. The rich phase diagram of the model was studied through DMRG, exact diagonalization, and a hard-core boson model. The phase diagram thus obtained presented three transition points. The first one is continuous and occurs at $J = 0.34$ between the Lieb-Mattis ferrimagnetic phase (F_1) and a ferrimagnetic phase (F_2) characterized by the condensation of the singlet component of spins at sites B_1 and B_2 of the same unit cell, with transverse critical antiferromagnetic correlations. At $J = 0.445$, a first-order transition to a phase characterized by spiral and predominantly AF correlations (*singlet spiral*) takes place. The number of singlets in the lattice is quantized before this transition, but is a continuous quantity afterwards, and can be envisioned by measuring the singlet density. Further, a continuous chain-ladder decoupling transition at $J = 0.91$ is observed. Above this value, the A spins present critical AF correlations following the asymptotic behavior observed in a linear chain, with power-law decay, while the ladder of B spins are short-range correlated with a finite correlation length, whose value is J -dependent, and nears the two-legged-ladder configuration (*decoupled chain ladder*).

As far as quantum rotors are concerned, the examination of the momentum correlations in Fig. 11 reveals that the system starts out with the FERRI phase which is the counterpart of phase F_1 of the spin system studied in Ref. 12. The double-cell variational MF energy plotted in Fig. 12 (a) exhibits a pattern quite similar to that of frustration F_1 , shown in Fig. 7 (a). But resorting to Fig. 11 with the help of Fig. 12 (b) (total aver-

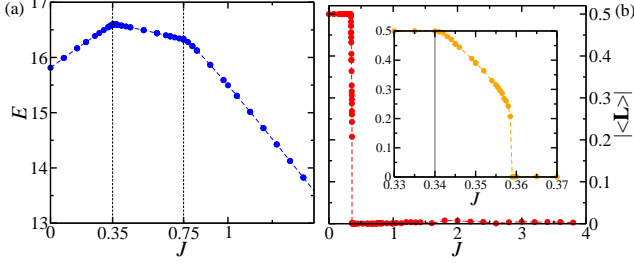


FIG. 12. (Color online) Quantum rotors by using the double-cell variational MF results for frustration F_2 : (a) energy and (b) expectation value of the total angular momentum per unit cell. The inset shows details of the phase transition around $J = 0.35$. Dashed lines are guides to the eye.

age momentum per unit cell), we can clear up the picture: in fact, at $J = 0.34$ it is reasonable to think that a second-order transition takes place giving rise to a narrow transient phase that corresponds to the phase F_2 (condensation of singlet components of spins at sites B of the same unit cell) for spin system and is best visualized through the inset in the latter figure, which shows the behavior of the total angular momentum. In this phase the momenta of the A sites keep their ferromagnetic configuration ($\langle \hat{\mathbf{L}}_{A_1} \cdot \hat{\mathbf{L}}_{A_2} \rangle = 0.25$) while the B momenta conform to a magnetic canted configuration. A first-order transition follows at $J \approx 0.36$ to a new state that should correspond to the phase *singlet spiral* of the respective spin system. With respect to the momenta at the A sites, the ferromagnetic configuration also prevails in this phase. The total angular momentum of the A sublattice exactly counterbalances that of the B sublattice, so that, as it happens for the spin system, a vanishing expectation value of the total angular momentum (spin) per unit cell occurs. Furthermore, upon inspecting the B correlations Fig. 11, this phase appears here to have also a semiclassical canted configuration, hence the name CANTED that we use to designate this QR phase together with the previous one. In the same manner for the spin system¹², the additional intercell interactions produce nonquantized values of the B momenta (see, for example, correlation $\langle \hat{\mathbf{L}}_{B_1} \cdot \hat{\mathbf{L}}_{B_3} \rangle$). The nonquantization verified in the spin system, which is a coherent superposition of singlet and triplet configurations, may rather be seen as manifestation of the symmetry-breaking of the invariance of the Hamiltonian under interchange of the B sites in the same cell brought about by the additional frustration. This is also clearly verified in the QR system. In the absence of the additional frustration, as is the case for frustration F_1 (Fig. 1 (a)), this symmetry stays unscathed, so that there is no singlet-triplet superposition: we have either a singlet or a triplet configuration per cell, but never both simultaneously, which was already the case for both spin and QR systems. Finally, as seen in Fig. 11, at $J = 0.75$, quantum fluctuations bring the sudden decoupling of the chain

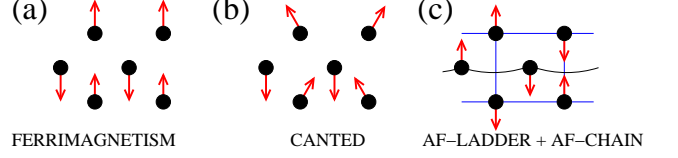


FIG. 13. (Color online) Illustration of the major QR ground states for frustration F_2 : (a) FERRI; (b) CANTED; (c) AF, which is composed of two decoupled 1D systems: a linear chain (A sites) and the two-legged ladder (B sites).

through another phase transition with first-order characteristics (in the spin system the transition is second-order), and the system settles into an antiferromagnetic (AF) phase, also marked by a vanishing expectation value of the total angular momentum per unit cell, as shown in Fig. 12 (b). In this phase the frustrated AB_2 chain splits into two decoupled chains, namely, an AF linear chain ($\langle \hat{\mathbf{L}}_{A_1} \cdot \hat{\mathbf{L}}_{A_2} \rangle = -0.75$) and an AF two-legged ladder ($\langle \hat{\mathbf{L}}_{B_1} \cdot \hat{\mathbf{L}}_{B_2} \rangle = \langle \hat{\mathbf{L}}_{B_1} \cdot \hat{\mathbf{L}}_{B_3} \rangle = \langle \hat{\mathbf{L}}_{B_1} \cdot \hat{\mathbf{L}}_{B_4} \rangle = -0.5$ and $\langle \hat{\mathbf{L}}_{B_1} \cdot \hat{\mathbf{L}}_{B_4} \rangle = 0.25$); the decoupling is seen through $\langle \hat{\mathbf{L}}_{A_1} \cdot \hat{\mathbf{L}}_{B_{3,4}} \rangle \approx 0$. In Fig. 13, we show a pictorial representation of the three major phases FERRI, CANTED and AF. With respect to this AF phase, our QR simulations evidently shed no light onto the criticality and short-rangedness of the linear and two-legged ladder chains, respectively. This phase corresponds to the *decoupled chain-ladder* system, which in turn has a vanishing total spin. The first-order transition at $J = 0.75$ may rather be seen as a manifestation of finite-size effects of our two-cell approach: the absence of many intermediate states preclude a smooth transition.

The average singlet density for this frustration pattern is shown in Fig. 14: the singlet number is quantized (except for the narrow interval around $J = 0.36$, until the frustration reaches the value $J = 0.75$, wherefrom the singlet number goes on nonquantized). We see that the QR system exhibits a four-phase pattern quite similar to that of the respective spin system, with the nature of all but the last phase transitions being similar in both systems. With respect to singlet quantization, we find agreement in the first and last phases (where singlet densities 0 and 0.7 are observed); in the intermediate phases no match is observed and again we impute this naturally to finite size effects of our two-cell approach, which hinder a discrete one-by-one singlet condensation. Also, because of the additional intercell frustration, it was not possible to form isolated singlet configurations as was the case for frustration F_1 .

In what follows, we provide a more detailed comparison between QR MF results and the spin-1/2 chain, in its quantum and classical versions. The phase diagram initially described of the spin-1/2 chain from Ref. 12 is summarized in Fig. 15 (a). The spiral phase can be exposed in a clear fashion through the pitch angle q ob-

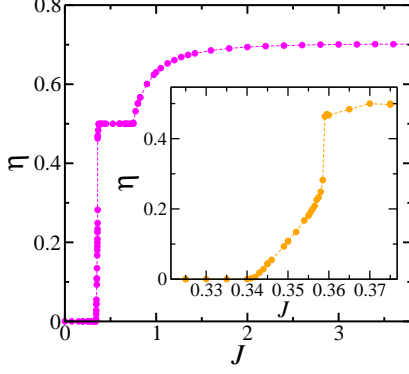


FIG. 14. (Color online) Quantum rotors with frustration F_2 : average singlet density per unit cell for the momentum correlations at B sites along the same rung of the ladder.

tained from the magnetic structure factor defined as

$$F(q) = \frac{1}{2N_c} \sum_{j,k} \langle \hat{\mathbf{S}}_j \cdot \hat{\mathbf{S}}_k \rangle e^{iq(j-k)}, \quad (20)$$

with $q = 2\pi n/(2N_c)$, for $n = 0, 1, 2, \dots, 2N_c - 1$, and $\mathbf{S}_j = \mathbf{A}_{(j+1)/2}$, if j is odd, while $\mathbf{S}_j = \mathbf{B}_{1,j/2} + \mathbf{B}_{2,j/2}$, if j is even, and here we are labeling the sites in a more convenient way: A_1 , B_{1l} , and B_{2l} just denote the sites A_1 , B_1 , and B_2 of the l th unit cell. In the Lieb-Mattis phase the ferrimagnetic order is indicated by a sharp peak at $q = \pi$ (a period-2 configuration); while in the decoupled phase, in which a period-4 structure is observed (see Fig. 13), there is a peak at $q = \pi/2$. These two situations are magnetic configurations commensurate with the lattice, while the spiral phase is indicated by a peak at a value of q between $q = \pi/2$ and $q = \pi$. In Fig. 15 (a) we display the behavior of q as a function of J for finite systems calculated through ED and DMRG. Finite size effects lead to a little shift in the transition point from the spiral phase to the decoupled phase, even though q can be clearly used to mark the spiral phase.

Motivated by these results, we consider the classical model in the space spanned by two parameters (in approach of Sec. III, one single parameter sufficed to explain the results): a canting angle θ between the B momenta at the same cell and the pitch angle q between the A momentum and the sum of the B momenta, associated with the spiral order. The classical fields are accordingly written as:

$$\begin{aligned} \mathbf{A}_l &= \cos[q(2l-1)]\mathbf{x} + \sin[q(2l-1)]\mathbf{z}; \\ \mathbf{B}_{1l} &= \cos(\theta)\cos(2ql)\mathbf{x} + \sin(\theta)(-1)^l\mathbf{y} \\ &\quad + \cos(\theta)\sin(2ql)\mathbf{z}, \text{ and} \\ \mathbf{B}_{2l} &= \cos(\theta)\cos(2ql)\mathbf{x} + \sin(\theta)(-1)^{l+1}\mathbf{y} \\ &\quad + \cos(\theta)\sin(2ql)\mathbf{z}, \end{aligned} \quad (21)$$

with $|\mathbf{A}_l| = |\mathbf{B}_{1l}| = |\mathbf{B}_{2l}| \equiv 1$, while \mathbf{x}, \mathbf{y} and \mathbf{z} are orthogonal unit vectors in the three-dimensional space. Substituting these fields in the classical version

of the Hamiltonian, Eq. (5), we get the energy function $E(q, \theta) \sim 4\cos q \cos \theta + J(\cos 2\theta + \cos 2q + 2\cos^2 \theta \cos 2q - 2\sin^2 \theta)$ and minimizing this function with respect to q and θ , we find that $\cos(\theta) = 1$ and $\cos(q) = \pi$ for $0 < J < (1/3)$, which is the classical version of the Lieb-Mattis phase found for $0 < J < 0.34$ in the quantum Hamiltonian, for both quantum rotors (FERRI phase) and spin system (Phase F1 of Ref. 12). For $(1/3) < J < 1$ we obtain

$$\cos(\theta) = \sqrt{\frac{1-J}{2J}}; \quad (22)$$

$$\cos(q) = -\cos(\theta), \quad (23)$$

which may be seen as the classical version of the CANTED phase ($0.34 \lesssim J \lesssim 0.75$) and of the spiral phase ($0.445 \lesssim J \lesssim 0.91$) found in Ref. 12. This phase holds some similarities with the second phase observed for the quantum rotors in the first single-site approach of Sec. III. Finally, for $J > 1$ the three chains are antiferromagnetically ordered with the B momenta lying in the y direction and the A momenta ordered in the z direction, which is the classical analog of the decoupled phase observed for $J > 0.75$ for the quantum rotors and for $J > 0.91$ for the spin system¹². Such phase does not exist in the single-site approach: it is only obtained asymptotically ($J \rightarrow \infty$). Therefore, the classical solution presents two critical points: $J_{c1,\text{classical}} = 1/3$ and $J_{c2,\text{classical}} = 1$, and the transitions remain second order. Also, the first-order transition at $J = 0.36$ ($J_t \approx 0.445$, for the spin systems) is not observed in the classical model. In fact, in the F_2 phase¹² ($0.34 \lesssim J \lesssim 0.445$) the number of singlets is quantized and the spiral peak is absent, while in the classical model the two orders coexist for $J_{c1,\text{classical}} < J < J_{c2,\text{classical}}$. This classical result is also indicated in Fig. 15 (a).

In Fig. 15 (b), we present the results of this classical interpretation for the momentum correlations. A direct relationship with Fig. 11 can be established: we have the classical counterparts of the FERRI phase ($J \leq 1/3$) and the AF phase ($J \geq 1$); the CANTED phase is but a gradual continuous transition between the FERRI and AF phases. Further, the decoupling transition in the classical model is clearly observed at $J = 1$ through the dot products indicated in the figure. Finally, we notice that when this classical approach is applied to frustration F_1 , the minimum energy configuration obtained is the same as that derived through the first classical model discussed in Sec. III.

V. SUMMARY AND CONCLUSIONS

In dealing with quantum rotors placed at the sites of an AB_2 chain we resorted to a cluster variational MF theory implemented via two distinct approaches, which yielded different results. First, we learned that the size of the Hilbert space could be considerably reduced without affecting results, with the proviso that the rotor states

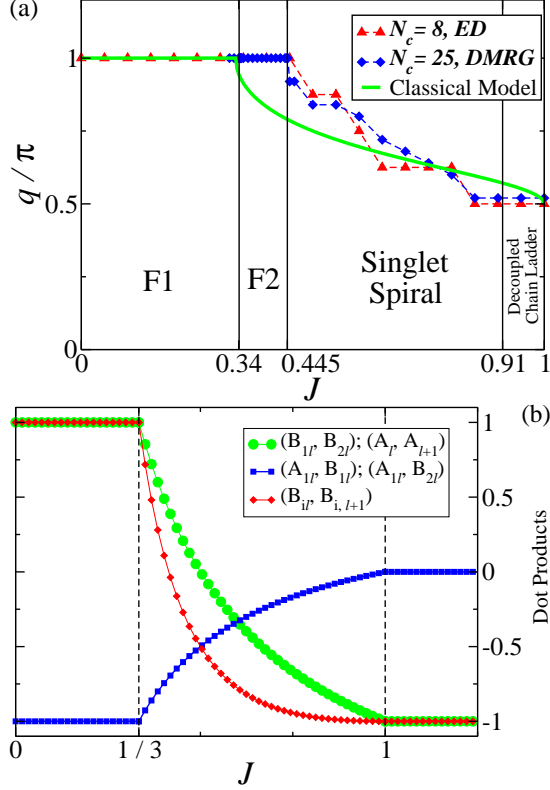


FIG. 15. (Color online) (a) Pitch angle for the quantum spin-1/2 model calculated through ED, DMRG, and for the minimum energy configuration of the classical vector model with two order parameters: q (pitch angle) and θ (canting angle). The transition points estimated in Ref. 12 are indicated. (b) Momentum dot products ($i = 1, 2$, and l denotes the unit cell) in the minimum energy configuration of the classical vector model.

should be kept possibly nearest ($\ell = 1/2$)-momentum states. That was attained by increasing the importance of the kinetic energy term in the Hamiltonian (by setting relatively high values of the coupling g), whenever needed. This was a most important fact for the computations in multiple-cell clusters in the second approach.

In the first approach the natural single-site MF theory was developed. A two-phase pattern was produced with the phase transition between them being of second order for $M = 0$ and of first order for $M = 1$. For $J \leq 1$, the Lieb-Mattis-like phase typical in the spin-1/2 system arose, and for $J \gg 1$, we observed the decoupling of the system where the momenta on the A sites tend to become uncorrelated with the momenta on the B sites, which in turn formed singlet-like pairs, while the decoupling of the A sites was a salient feature laid bare by this approach, much like the dimer-monomer phase in Ref. 12. A classical interpretation was laid down that conformed to our QR numerical findings, inclusively showing how the fixed coupling momentum-position turns the second-order transition into a first-order one, when $M = 1$.

However, we were not able to provide a reasonable quantum picture that could relate to the known behavior of the corresponding quantum AB_2 chain. Furthermore, treated this way the system was not able to essentially tell apart frustration F_1 from frustration F_2 and this alone constituted a major setback. So, all this was a reminder that the main goal of our work still remained to be achieved.

In our last step, we then improved the former approach by producing a cluster (double-cell) variational MF theory in which the trial Hamiltonian acts on the space composed of the tensor product of the respective local subspaces of the six sites at two neighboring unit cells. The gist of this theory stands on the important fact that it allows the construction of the two-point correlations $\langle \hat{X}_i \cdot \hat{Y}_j \rangle$ between any pairs of operators acting on sites i, j of the cluster. This afforded us the observation of quantum features inherent in the system, as well as to distinguish between both frustrations F_1 and F_2 . For the construction of this more complex “system”, we relied on the availability of processing capacity to carry out the numerical implementation.

For frustration F_1 , besides the QR numerical simulation, we carried out ED on the spin-1/2 diamond chain using a system with 28 sites and calculated the correlation functions between spin at a central cluster, as well as other relevant physical quantities. Upon confronting with the QR results, we verified that the QR phase diagrams obtained through numerical implementation of the double-cell MF variational approach exhibited a sequence of phases analogous to those of the spin chains, with phase transitions of the same nature. We therefore produced the FERRI-TD-DM phase sequence, with first order transitions, which is in essence the phase diagram of Ref. 10. The transition point FERRI-TD at $J = 0.68$ is somewhat displaced, but the transition point TD-DM at $J = 2$ was exactly calculated by our approach.

For frustration F_2 , we obtained a phase diagram in good agreement with the results of Ref. 12 on the respective spin-1/2 chains, endowed with the equivalent frustration pattern: FERRI, CANTED, and AF which are associated with the phases F1, F2/Singlet, and decoupled ladder chain, respectively, of the spin model. Notwithstanding, the criticality of the A spins correlations manifests itself here as an AF magnetic ordering due to finite-size effects. For the same reason, we can not probe the short-rangedness of the correlation functions between B momenta. We also produced ED as well as DMRG results that helped us to visualize the spiral phase in the spin system, and derived an insightful classical interpretation.

VI. ACKNOWLEDGMENTS

This work was supported by CNPq, FACEPE, CAPES, and Finep (Brazilian agencies).

Appendix A: The Basis of Monopole Harmonics States

In this appendix we provide the derivation of the matrix elements in the monopole harmonics basis representation for the $\hat{\mathbf{n}}$ operator, for any value of q . This derivation was done straightforwardly based solely on the definitions⁶ and the properties of the Jacobi polynomials. Thus the following recurrence relations of the Jacobi polynomials³⁴ can be established, valid for all q :

$$\begin{aligned} l \left[\frac{(l+m+1)(l-m+1)(l+q+1)(l-q+1)}{(2l+3)(l+m)(l-m)} \right]^{1/2} Y_{q,l+1,m}(\theta, \phi) = \\ [l(l+1)\cos\theta + 2mq] \left[\frac{2l+1}{(l+m)(l-m)} \right]^{1/2} Y_{q,l,m}(\theta, \phi) \\ - (l+1) \left[\frac{(l+q)(l-q)}{2l-1} \right]^{1/2} Y_{q,l-1,m}(\theta, \phi), \end{aligned} \quad (\text{A1})$$

$$\begin{aligned} [(1-x^2)e^{-i\phi}] \left[\frac{1}{(l+m)(l+m-1)} \right]^{1/2} Y_{q,l-1,m+1}(\theta, \phi) = \\ \frac{1}{l} \left[\frac{(l+q)(l-q)(l-m-1)(l-m)}{(2l+1)(2l-1)(l+m)(l+m-1)} \right]^{1/2} Y_{q,l,m}(\theta, \phi) \\ - \frac{q}{l(l-1)} \left[\frac{l-m-1}{l+m-1} \right] Y_{q,l-1,m}(\theta, \phi) \\ - \frac{1}{l-1} \left[\frac{(l+q-1)(l-q-1)}{(2l-3)(2l-1)} \right]^{1/2} Y_{q,l-2,m}(\theta, \phi), \end{aligned} \quad (\text{A2})$$

$$\begin{aligned} [(1-x^2)e^{i\phi}] \left[\frac{1}{(l-m+1)(l-m)} \right]^{1/2} Y_{q,l,m-1}(\theta, \phi) = \\ - \frac{q(l+m)}{l(l+1)} \left[\frac{1}{(l+m)(l-m)} \right]^{1/2} Y_{q,l,m}(\theta, \phi) \\ - \frac{1}{(l+1)} \left[\frac{(l+m)(l+m+1)(l+q+1)(l-q+1)}{(2l+1)(2l+3)(l-m+1)(l-m)} \right]^{1/2} Y_{q,l+1,m}(\theta, \phi) \\ + \frac{1}{l} \left[\frac{(l+q)(l-q)}{(2l+1)(2l-1)} \right]^{1/2} Y_{q,l-1,m}(\theta, \phi). \end{aligned} \quad (\text{A3})$$

Next we use the orthogonality relation for the monopole harmonics and specialize in the case $q = \frac{1}{2}$ to get the respective non-zero matrix elements for the operator $\hat{\mathbf{n}}$, used in this work. So, we have set $\hat{n}_{\pm} = \hat{n}_x \pm i\hat{n}_y$, which is defined similarly to \hat{L}_{\pm} , where we have the following: $x = \cos\theta$ and $\hat{n}_z \leftrightarrow \cos\theta$, $\hat{n}_+ \leftrightarrow e^{i\phi}\sin\theta$ (the matrix elements of \hat{n}_- are obtained by complex conjugation): $\langle \frac{1}{2}, l, m | \hat{n}_z | \frac{1}{2}, l, m \rangle = -\frac{m}{l(2l+2)}$; $\langle \frac{1}{2}, l, m | \hat{n}_z | \frac{1}{2}, l-1, m \rangle = \frac{1}{2l}\sqrt{(l-m)(l+m)}$;

$$\begin{aligned} \langle \frac{1}{2}, l, m | \hat{n}_+ | \frac{1}{2}, l, m-1 \rangle &= -\frac{1}{2l(l+1)}\sqrt{(l-m+1)(l+m)}; \\ \langle \frac{1}{2}, l, m | \hat{n}_+ | \frac{1}{2}, l-1, m-1 \rangle &= -\frac{1}{2l}\sqrt{(l+m)(l+m-1)}; \\ \text{and } \langle \frac{1}{2}, l, m | \hat{n}_+ | \frac{1}{2}, l+1, m-1 \rangle &= \frac{1}{2(l+1)}\sqrt{(l-m+1)(l-m+2)}. \end{aligned}$$

For the sake of completeness, we write down the matrix elements for the operator $\hat{\mathbf{L}}$, valid for all q , obtained through the ladder-operator and eigenvalue relations for the monopole harmonics: $\langle l, m | \hat{L}^2 | l, m \rangle = l(l+1)$, $\langle l, m | \hat{L}_z | l, m \rangle = m$, and $\langle l, m | \hat{L}_+ | l, m-1 \rangle = [(l+m)(l-m+1)]^{1/2}$.

¹ A. Auerbach, *Interacting Electrons and Quantum Magnetism* (Springer-Verlag, New York, 1998).

² S. Sachdev, *Quantum Phase Transitions* (Cambridge University Press, Cambridge-UK, 2001).

- ³ C. J. Hamer, J. B. Kogut, and L. Susskind, Phys. Rev. D, **19**, 3091 (1979).
- ⁴ F. D. M. Haldane, Phys. Lett. **93A**, 464 (1983); F. D. M. Haldane, Phys. Rev. Lett. **50**, 1153 (1983).
- ⁵ R. Shankar and N. Read, Nucl. Phys. B **336**, 457 (1990).
- ⁶ T. T. Wu and C. N. Yang, Nucl. Phys. B **107**, 365 (1976).
- ⁷ S. Sachdev and T. Senthil, Ann. Phys. **251**, 76 (1996).
- ⁸ A. Imambekov, M. Lukin, and E. Demler, Phys. Rev. Lett. **93**, 120405 (2004).
- ⁹ T. P. Polak and T. K. Kopeć, Phys. Rev. B **76**, 094503 (2007).
- ¹⁰ K. Takano, K. Kubo, and H. Sakamoto, J. Phys.: Condens. Matter **8**, 6405 (1996).
- ¹¹ T. Tonegawa, K. Okamoto, T. Hikihara, Y. Takahashi, and M. Kaburagi, J. Phys. Soc. Jpn. **69**, 332 (2000).
- ¹² R. R. Montenegro-Filho and M. D. Coutinho-Filho, Phys. Rev. B **78**, 014418 (2008).
- ¹³ K. Sano and K. Takano, J. Phys. Soc. Jpn. **69**, 2710 (2000); K. Okamoto, T. Tonegawa, Y. Takahashi, and M. Kaburagi, J. Phys.: Condens. Matter **11**, 10485 (1999); H. Niggemann, G. Uimin, and J. Zittartz, J. Phys.: Condens. Matter **9**, 9031 (1997).
- ¹⁴ K. Okamoto, T. Tonegawa, and M. Kaburagi, J. Phys.: Condens. Matter **15**, 5979 (2003).
- ¹⁵ N. B. Ivanov, J. Richter, and J. Schulenburg, Phys. Rev. B **79**, 104412 (2009).
- ¹⁶ C. Lanczos, J. Res. Natl. Bur. Stand. **45**, 255 (1950).
- ¹⁷ S. R. White, Phys. Rev. B **48**, 10345 (1993); U. Schollwöck, Rev. Mod. Phys. **77**, 259 (2005).
- ¹⁸ H. Kikuchi, Y. Fujii, M. Chiba, S. Mitsudo, T. Idehara, T. Tonegawa, K. Okamoto, T. Sakai, T. Kuwai, and H. Ohta, Phys. Rev. Lett. **94**, 227201 (2005); See also K. C. Rule, A. U. B. Wolter, S. Süllow, D. A. Tennant, A. Brühl, S. Köhler, B. Wolf, M. Lang, and J. Schreuer, Phys. Rev. Lett. **100**, 117202 (2008).
- ¹⁹ M. Matsuda, K. Kakurai, A. A. Belik, M. Azuma, M. Takano, and M. Fujita, Phys. Rev. B **71**, 144411 (2005).
- ²⁰ Y. Hosokoshi, K. Katoh, Y. Nakazawa, H. Nakano, and K. Inoue, J. Am. Chem. Soc. **123**, 7921 (2001).
- ²¹ For a review see: M. D. Coutinho-Filho, R. R. Montenegro-Filho, E. P. Raposo, C. Vitoriano, and M. H. Oliveira, J. Braz. Chem. Soc. **19**, 232 (2008).
- ²² A. M. S. Macêdo, M. C. dos Santos, M. D. Coutinho-Filho, and C. A. Macêdo, Phys. Rev. Lett. **74**, 1851 (1995); G.-S. Tian and T.-H. Lin, Phys. Rev. B **53**, 8196 (1996).
- ²³ G. Sierra, M. A. Martín-Delgado, S. R. White, D. J. Scalapino and J. Dukelsky, Phys. Rev. B **59**, 7973 (1999).
- ²⁴ C. Vitoriano, M. D. Coutinho-Filho, and E. P. Raposo, J. Phys. A: Math. Gen. **35**, 9049 (2002);
- ²⁵ F. C. Alcaraz and A. L. Malvezzi, J. Phys. A: Math. Gen. **30**, 767 (1997); E. P. Raposo and M. D. Coutinho-Filho, Phys. Rev. Lett. **78**, 4853 (1997); E. P. Raposo and M. D. Coutinho-Filho, Phys. Rev. B **59**, 14384 (1999); M. A. Martín-Delgado, J. Rodriguez-Laguna, and G. Sierra, Phys. Rev. B **72**, 104435 (2005).
- ²⁶ C. Vitoriano, F. B. de Brito, E. P. Raposo, and M. D. Coutinho-Filho, Mol. Cryst. Liq. Cryst. **374**, 185 (2002); T. Nakanishi and S. Yamamoto, Phys. Rev. B **65**, 214418 (2002); S. Yamamoto and J. Ohara, Phys. Rev. B **76**, 014409 (2007).
- ²⁷ R. R. Montenegro-Filho and M. D. Coutinho-Filho, Physica A **357**, 173 (2005).
- ²⁸ M. H. Oliveira, M. D. Coutinho-Filho, and E. P. Raposo, Phys. Rev. B **72**, 214420 (2005).
- ²⁹ R. R. Montenegro-Filho and M. D. Coutinho-Filho, Phys. Rev. B **74**, 125117 (2006), and references therein.
- ³⁰ H. B. Callen, *Thermodynamics and an Introduction to Thermostatistics* (John Wiley & Sons Inc, New York-NY, 1985); R. P. Feynman, *Statistical Mechanics—A Set of Lectures* (The Benjamin Cummings Publishing Company Inc, Reading-MA, 1972).
- ³¹ C. S. O. Yokoi, M. D. Coutinho-Filho, and S. R. Salinas, Phys. Rev. B **24**, 4047 (1981).
- ³² *Numerical Recipes Inc: The Art of Scientific Computing* (Cambridge University Press, Cambridge-UK, 1992).
- ³³ E. H. Lieb and D. Mattis, J. Math. Phys. **3**, 749 (1962).
- ³⁴ A. Ederlyi (editor), *Higher Transcendental Functions (Bateman Project)* (McGraw-Hill Book Company Inc, New York-NY, 1953).